Achiral symmetry breaking and positive Gaussian modulus lead to scalloped colloidal membranes

Thomas Gibaud[a,b], C. Nadir Kaplan[a,c], Prerna Sharma[a,d], Mark J. Zakhary[a], Andrew Ward[a,e], Rudolf Oldenbourg[f,g], Robert B. Meyer[a], Randall D. Kamien[h], Thomas R. Powers[g,i], and Zvonimir Dogic[a,1]

[a]The Martin Fisher School of Physics, Brandeis University, Waltham, MA 02454; [b]Université de Lyon, Ens de Lyon, Université Claude Bernard, CNRS, Laboratoire de Physique, F-69342 Lyon, France; [c]John A. Paulson School of Engineering and Applied Sciences, Harvard University, Cambridge, MA 02138; [d]Department of Physics, Indian Institute of Science, Bangalore 560012, India; [e]Program in Cellular and Molecular Medicine, Boston Children's Hospital, Boston, MA 02115; [f]Marine Biological Laboratory, Woods Hole, MA 02543; [g]Department of Physics, Brown University, Providence, RI 02912; [h]Department of Physics and Astronomy, University of Pennsylvania, Philadelphia, PA 19104; and [i]School of Engineering, Brown University, Providence, RI 02912

Edited by David A. Weitz, Harvard University, Cambridge, MA, and approved March 13, 2017 (received for review October 20, 2016)

In the presence of a nonadsorbing polymer, monodisperse rod-like particles assemble into colloidal membranes, which are one-rod-length–thick liquid-like monolayers of aligned rods. Unlike 3D edgeless bilayer vesicles, colloidal monolayer membranes form open structures with an exposed edge, thus presenting an opportunity to study elasticity of fluid sheets. Membranes assembled from single-component chiral rods form flat disks with uniform edge twist. In comparison, membranes composed of a mixture of rods with opposite chiralities can have the edge twist of either handedness. In this limit, disk-shaped membranes become unstable, instead forming structures with scalloped edges, where two adjacent lobes with opposite handedness are separated by a cusp-shaped point defect. Such membranes adopt a 3D configuration, with cusp defects alternatively located above and below the membrane plane. In the achiral regime, the cusp defects have repulsive interactions, but away from this limit we measure effective long-ranged attractive binding. A phenomenological model shows that the increase in the edge energy of scalloped membranes is compensated by concomitant decrease in the deformation energy due to Gaussian curvature associated with scalloped edges, demonstrating that colloidal membranes have positive Gaussian modulus. A simple excluded volume argument predicts the sign and magnitude of the Gaussian curvature modulus that is in agreement with experimental measurements. Our results provide insight into how the interplay between membrane elasticity, geometrical frustration, and achiral symmetry breaking can be used to fold colloidal membranes into 3D shapes.

self-assembly | membranes | liquid crystals | Gaussian curvature | chirality

The possible configurations and shapes of 2D fluid membranes can be described by a continuum energy expression that accounts for the membrane's out-of-plane deformations as well as the line tension associated with the membrane's exposed edge (1, 2). Because an arbitrary deformation of a thin layer can have either mean and/or Gaussian curvature, the full theoretical description of membranes, in principle, requires two parameters, the bending and Gaussian curvature moduli. However, lipid bilayers almost always appear as edgeless 3D vesicles, which further simplify theoretical modeling. In particular, integrating Gaussian curvature over any simply closed surface yields a constant (3). Thus, the shape fluctuations of a closed vesicle only depend on the membrane-bending modulus. Consequently, experiments that interrogated mechanics or shape fluctuations of vesicles provided extensive information about the membrane curvature modulus and how it depends on the structure of the constituent particles (4–6). In comparison, significantly less is known about the Gaussian modulus, despite the significant role it plays in fundamental biological and technological processes such as pore formation as well as vesicle fusion and fission (7–11).

Recent experiments have demonstrated that, in the presence of a depleting agent, monodisperse rods robustly assemble into one-rod-length–thick 2D membranes, with in-plane liquid order (12–16). Although more than two orders of magnitude thicker than lipid membranes, the deformations of both colloidal monolayers and lipid bilayers are described by the same elastic energy (17). However, in contrast to conventional membranes that fold into 3D vesicles, colloidal membranes appear as open structures. This presents a unique opportunity to explore the elasticity of 2D fluid sheets, a geometry for which both the Gaussian modulus and edge energy play an important role. Here, we explore the possible shapes of colloidal membranes and demonstrate an unexpected connection between the membrane's edge structure, Gaussian curvature, and the chirality of the constituent rods.

The semicircular edge profile requires twisting of the rods at the edge, and this twist penetrates into the membrane interior over a characteristic length scale (16, 18, 19). For membranes composed of single-component chiral rods, the handedness of the edge twist along the entire circumference is uniform and dictated by the microscopic chirality of the constituent rods. With decreasing chirality, which is accomplished by mixing rods of opposite handedness, flat 2D circular membranes become unstable, and instead develop complex scalloped edges. In this limit, edge-bound rods exhibit achiral symmetry breaking, forming domains of opposite twist that are separated by cusp-like point defects, where the membrane escapes into the third dimension. The exact structure of the scalloped edge is determined by the competition between the line tension and the Gaussian curvature modulus. Line tension favors circular flat membrane

Significance

A number of essential processes in biology and materials science, such as vesicle fusion and fission as well as pore formation, change the membrane topology and require formation of saddle surfaces. The energetic cost associated with such deformations is described by the Gaussian curvature modulus. We show that flat 2D colloidal membranes composed of achiral rods are unstable and spontaneously form scalloped edges. Quantitative analysis of such instability estimates the Gaussian curvature modulus of colloidal membranes. The measured sign and magnitude of the modulus can be explained by a simple excluded volume argument that was originally developed for polymeric surfactants.

Author contributions: T.G., R.B.M., and Z.D. designed research; C.N.K. developed the theoretical model of defect interactions; R.D.K. and T.R.P. provided theoretical estimate of the Gaussian curvature modulus; R.B.M. contributed to the theoretical model; T.G., C.N.K., P.S., M.J.Z., and A.W. performed research; R.O. contributed new reagents/analytic tools; P.S. acquired coalescence movies; A.W. contributed optical-tweezer measurements; R.O. contributed microscopy expertise; T.G., C.N.K., and T.R.P. analyzed data; and T.G., C.N.K., T.R.P., and Z.D. wrote the paper.

The authors declare no conflict of interest.

This article is a PNAS Direct Submission.

[1]To whom correspondence should be addressed. Email: zdogic@brandeis.edu.

This article contains supporting information online at www.pnas.org/lookup/suppl/doi:10.1073/pnas.1617043114/-/DCSupplemental.

that minimizes the exposed edge. In comparison, an undulating scalloped edge creates excess Gaussian curvature and is thus favored by membranes that have positive Gaussian moduli. Thus, observations of scalloped edges demonstrate that Gaussian modulus of colloidal membranes is positive. Tuning the membrane's chiral composition effectively controls the interactions between cusp defects that can be either attractive or repulsive. Measurements of these interactions leads to an estimate of the Gaussian curvature modulus that is in agreement with the predictions of a simple theoretical model.

Structure of Colloidal Membranes

Our experimental model system is a colloidal membrane that spontaneously assembles in a mixture of dilute monodisperse rod-like viruses and nonadsorbing polymer dextran. The viruses alone interact through repulsive screened electrostatic repulsions (20). Addition of nonadsorbing polymer induces attractive depletion interactions that lead to assembly of colloidal membranes, equilibrium structures consisting of a one-rod-length–thick monolayer of aligned rods with a fluid-like internal structure (12). For our experiments, we use wild-type filamentous virus (*fd-wt*) and *fd*-Y21M that differs from its wild-type counterpart by a point mutation in the major coat protein (21). Both viruses have comparable contour length (22); however, studies of bulk cholesteric phase demonstrate that *fd-wt* forms a left-handed cholesteric structure, whereas *fd*-Y21M forms a right-handed one (Fig. 1*A*) (23–25). *fd-wt*/*fd*-Y12M mixture forms a homogeneous cholesteric phase with a pitch that depends on the ratio, $x_{fd} \equiv n_{fd}/(n_{fd} + n_{fdY21M})$, where n_{fd} and n_{fdY21M} are the concentration of *fd-wt* and *fd*-Y21M rods, respectively (24). The associated twist wave-number varies monotonically and smoothly from positive (right-handed) to negative (left-handed). It changes sign at $x_{fd} = 0.26$, the ratio at which the virus mixture is effectively achiral.

The structure of the colloidal membrane's edge is determined by the balance of the surface energy associated with the rod-depletion polymer interface and the elastic distortion energy originating from the nonuniform packing of rods within the membrane. The surface energy favors a curved edge profile, whereas elastic distortions favor a squared edge (15, 16, 19, 26). For *fd*-virus–based colloidal membranes, the surface energy dominates; consequently, the membrane's edge is curved and the edge-bound rods have to twist away from the membrane normal to fit the rounded profile imposed by the surface tension. Furthermore, the structure of the edge profile, and in particular the twist penetration depth λ_t, is independent of the chirality of the viruses; however, the chirality of the viruses does influence the effective edge tension of the membrane (19).

The tilting of edge-bound rods away from the membrane normal results in structural and optical anisotropy in the *x*–*y* plane (Fig. 1 *B* and *C*) (15, 16, 19). The optical anisotropy can be quantified by 2D-LC-PolScope that yields images where each pixel's intensity is proportional to the 2D projection in the *x*–*y* plane of the retardance, *R* (27). The resulting twist at the edge penetrates into the membrane interior over a characteristic length scale (18). A radial retardance profile yields a twist penetration length that is significantly different between *fd*-Y21M and *fd-wt* (Fig. 1*F*). However, the 2D projection of the retardance map does not reveal the handedness of the edge twist. To extract this information, we use 3D-LC-PolScope (28). Briefly, a microlens array is introduced into the back focal plane of the objective of the 2D-LC-PolScope, producing a grid of conoscopic images on the CCD camera. Each conoscopic image determines the local orientation of rods. An azimuthally symmetric retardance

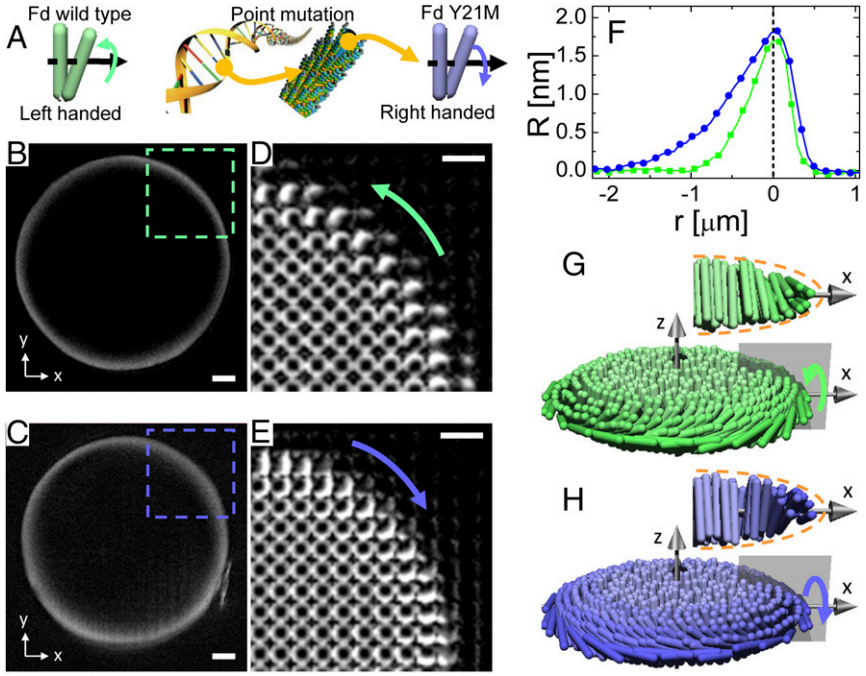

Fig. 1. Microscopic chirality of constituent rods determines preferred twist at the membrane's edge. (*A*) Bacteriophage *fd-wt* is a rod-like molecule with left-handed chirality (green). A single point mutation of the major coat protein switches the microscopic chirality, yielding *fd*-Y21M (blue). (*B* and *C*) 2D-LC-PolScope images of *fd-wt* and *fd*-Y21M colloidal membranes. The local twist at the membrane's edge results in optical retardance that is visualized with polarization techniques. The retardance is coded in a linear grayscale that varies from $R = 0$ nm (black) to $R = 3$ nm (white). (*D* and *E*) 3D-LC-PolScope image of *fd-wt* and *fd*-Y21M membranes reveals that the twist of the edge-bound rods is left-handed for *fd-wt* and right-handed for *fd*-Y21M. (*F*) Comparison of the radial retardance profile, $R(r)$, for both *fd-wt* and *fd*-Y21M membranes. The membrane interior is located at $r < 0$ and its edge is at $r = 0$. For *fd-wt* membranes, the twist penetration length is $\lambda_t = 0.45 \pm 0.05$ μm, whereas for *fd*-Y21M membranes it is $\lambda_t = 1.00 \pm 0.11$ μm. (*G* and *H*) Schematics of *fd-wt* and *fd*-Y21M colloidal membranes. (Scale bars: 2 μm.)

profile with a dark spot in the center indicates that rods at that locality are oriented along the z axis. A shift of the zero-retardance spot away from the center of a conoscopic image yields the magnitude of the local virus tilting, whereas its radial position indicates the 3D direction of the birefringence vector. 3D-LC-PolScope images show that *fd-wt* membranes composed of *fd-wt* and *fd*-Y21M viruses are right- and left-handed, respectively (Fig. 1 *D* and *E*).

Weakly Chiral Rod Mixtures Lead to Scalloped Membranes

Next, we examine the structure of colloidal membranes assembled from a mixture of *fd-wt* and *fd*-Y21M. The difference in their contour length of less than a few percent is not sufficient to induce lateral phase separation (29); instead, we observe uniformly mixed membranes throughout the entire range of parameters studied here (Fig. 2). The membranes are stable for a wide range of depletant concentrations and for all ratios x_{fd} (Fig. 2*A*). The twist at the membrane edge is right-handed at low x_{fd} and left-handed at high x_{fd}. Surprisingly, for intermediate x_{fd} ($0.04 < x_{fd} < 0.45$), we no longer observe flat circular membranes; instead, the membrane's entire edge becomes decorated with a series of outward protrusions that are terminated by cusp-like defects (Fig. 2*B*). Furthermore, z scans indicate that such scalloped membranes are not flat but have a distinct 3D structure where a cusp point defect located below the membrane is always followed by a defect located above the same plane (Fig. 3).

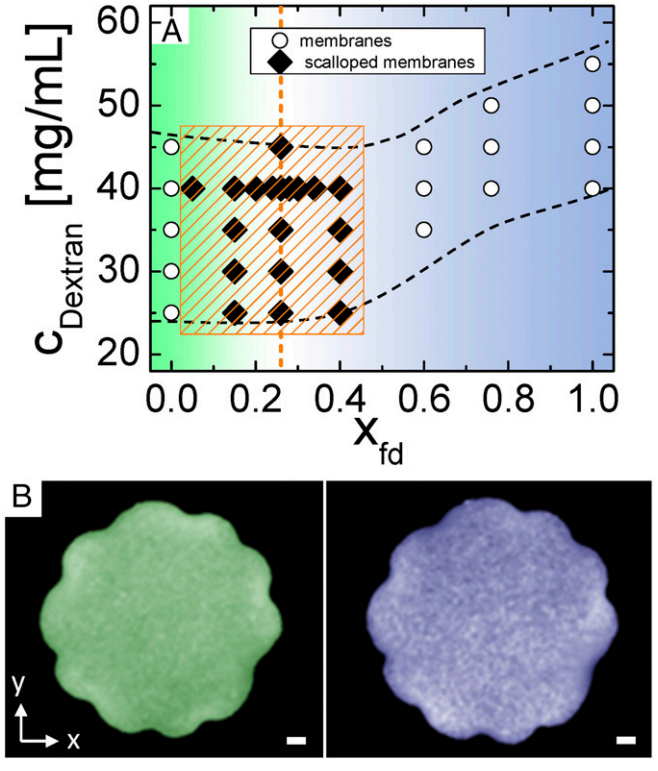

Fig. 2. Colloidal membranes assembled from *fd-wt*/*fd*-Y21M mixtures. (*A*) Phase diagram of the *fd-wt*/*fd*-Y21M mixture as a function of the number fraction x_{fd} versus the depletant concentration $C_{Dextran}$. We observe scalloped membranes around the achiral ratio $x_{fd} = 0.26$ (vertical dashed line) in the orange-shaded region. (*B*) Dual-view fluorescence imaging of a scalloped membrane at $x_{fd} = 0.26$ and $C_{Dextran} = 40$ mg/mL. *fd-wt* viruses are labeled with the fluorescent dye Alexa 488 (*Left*) and *fd*-Y21M viruses with DyLight-550 (*Right*). The density distribution of both *fd-wt* (*Left*) and *fd*-Y21M (*Right*) is homogeneous throughout the membrane interior. (Scale bars: 2 μm.)

2D-LC-Polscope images of the scalloped membranes demonstrate that rods at the edge of each outward protrusion have the same twist penetration length (Fig. 3 *A* and *B* and Fig. S1*A*). However, 3D-LC-Polscope reveals that adjacent protrusions have alternating left- and right-handed twist (Fig. 3*C*). The regions of opposite twist are separated by cusp-like point defects. Because each protrusion is always accompanied with two adjacent point defects alternating above and below the monolayer plane, there can only be an even number of cusp defects along the membrane circumference. The combined z-stack and 3D-LC-PolScope images allow us to schematize the edge structure of the scalloped membranes, which is more intricate compared with the edge structure of chiral colloidal monolayers studied previously (Fig. 3 *D*–*F*). The formation of the scalloped membranes is the direct consequence of molecular chirality, because scalloped membranes appear in the limit of weak chirality, that is, between $0.04 < x_{fd} < 0.4$ (Fig. 2*A*).

In principle, there could be localized demixing of the two rods species, where *fd-wt* would preferentially localize at the edges with a left-handed twist, and *fd*-Y21M at the edges with opposite twist. This was not observed experimentally. We labeled all *fd-wt* rods with a fluorescent dye (Alexa 488) and *fd*-Y21M rods with fluorescent dye (Dylight 550). Using dual-view fluorescence, a technique that allows us to simultaneously image *fd-wt* and *fd*-Y21M fluorescent rods, we observe that, within experimental error, membranes in bulk and at the edges remain homogeneously mixed for all x_{fd}, even within the outward protrusion (Fig. 2*B* and Movies S1 and S2). Furthermore, using previously described techniques (18, 19), we have measured how the twist penetration length λ_t, the interfacial tension γ, and the edge bending rigidity k_b depend on x_{fd}. For scalloped membranes, we find that outward protrusions with either handedness had the same λ_t (Fig. S2) and γ and k_b that could not be distinguished within experimental error. Additionally, these quantities varied continuously from $x_{fd} = 0$ to $x_{fd} = 1$, which also indicates mixture homogeneity (Fig. S1).

Membrane Coalescence Generates Cusp-Like Deformations

Lateral coalescence of colloidal membranes can lead to the formation of unconventional defect structures. For example, two laterally coalescing membranes of the same handedness can trap 180° of twist, resulting in a π-wall line defect (26). To elucidate a possible mechanism that leads to the formation of cusps in scalloped membranes, we observed membrane coarsening by using an angled-light 2D-LC-PolScope. This technique differs from conventional 2D-LC-PolScope; instead of having the light source aligned with the z axis, the almost closed aperture associated with the back focal plane is translated away from the optical center, resulting in the plane waves illuminating the sample at an angle. This in turn reveals the handedness of the local rod twisting. We define a coordinate system in which the optical axis lies along the z direction, and the membrane lies in the x–y plane (Fig. 4*A*). The aperture of the condenser back focal plane is placed so that the incident illumination is tilted in the x–z plane. It follows that the rods within a membrane along the y axis (dashed line in Fig. 4*B*) exhibit a variable tilt with the respect to the illumination plane. The regions where rods are perpendicular to the plane of the illuminating wave will exhibit no optical retardance, whereas retardance will increase with an increasing tilt of rods away from the angle of the incident light. As a result, the lower edge of a right-handed membrane exhibits reduced retardance (relative to the rods in the bulk) as the viruses tilt toward the light source, whereas the upper edge exhibits increased retardance due to the rods tilting away from the light source (Fig. 4*B*). By the same reasoning, a left-handed membrane will exhibit the opposite behavior, with darker and brighter regions at the top and bottom of the membrane along the y axis, respectively (Fig. 4*C*). This technique allows us to distinguish between left- and right-handed

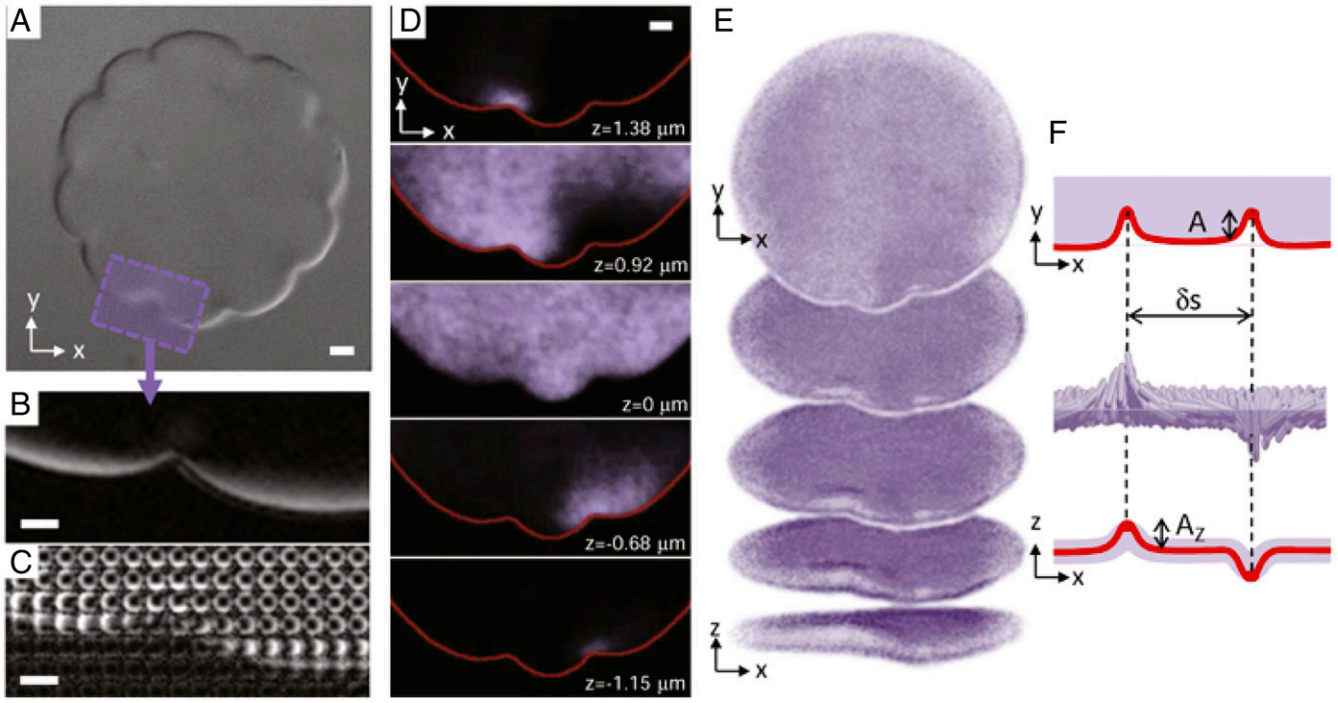

Fig. 3. Structure of scalloped membranes. (*A*) Differential interference contrast (DIC) image of a scalloped membrane formed in a *fd-wt* /*fd*-Y21M mixture at the achiral ratio $x_{fd} = 0.26$ ($C_{dextran} = 40$ mg/mL). The membrane's edge is decorated with a series of cusps separated by local outward protrusions. (*B*) 2D-LC-PolScope image of the membrane profile around a point defect. The twist penetration length λ_t is identical on both sides of the cusp (Fig. S2). (*C*) 3D-LC-PolScope image of the membrane profile surrounding the defect. The viruses have opposite twist on either side of the point defect. (*D*) *Z* scan of the scalloped membranes under confocal microscopy. The point defects alternate above and below the monolayer plane. (*E*) Reconstruction of the membrane based on the confocal images. (*F*) Schematic of a point defect inferred from the measurements in *C* and *D*. The protrusion amplitude in the *xy* plane is denoted by *A* and the cusp height by A_z. (Scale bars: 2 μm.)

membrane edges with a higher spatial resolution than 3D-LC-PolScope.

For $0.04 < x_{fd} < 0.45$, in the early stages of the sample maturation, we observe circular membranes of either edge handedness, indicating spontaneously broken achiral symmetry. Over time, the intermediate-sized membranes with mixed edge twist continue to coalesce. When two membranes with the same handedness merge, we observe the formation of either a π-wall or an array of pores at the coalescence junction, as was discussed previously (Fig. 4*B* and Movie S3). By contrast, as the two proximal edges of a membrane pair with the opposite twist rupture, the adjoining neck widens and the twist of the edge-bound rods is expelled by aligning constituent rods with the membrane normal (Fig. 4*C* and Movie S4). This coalescence process leads to a daughter membrane that has two outward protrusions and two cusp defects at which the twist of edge-bound rods switches handedness. Once formed, the cusp defects remain stable indefinitely. An outward protrusion with a pair of defects can also be imprinted into the edge using optical tweezers (Fig. 4*D* and Movie S5). The method, which allows for robust engineering of cusp defects, consists of pulling the twisted ribbons out of the membrane. The first few steps of this procedure are similar to the previously studied disk-to-ribbons transition (19). Subsequently, reversing the direction of the optical trap and dragging it toward the membrane leads to the formation of defect pairs.

Effective Interactions Between Adjacent Point Defects

The structure of the scalloped edges greatly depends on the number fraction x_{fd} and how close the membrane is to the achiral limit ($x_{fd} = 0.26$). At the boundary of stability of scalloped membranes, near $x_{fd} = 0.04$ or 0.45, a pair of point defects remains bound to each other at a well-defined distance (Fig. 5*A*). In comparison, close to the achiral limit the defect pair freely moves along the edge and the total circumference of each outward protrusion exhibits significant fluctuations (Movie S6). These observations can be explained by the chiral control of membrane line tension (19). Increasing the rod chirality raises the free energy of the untwisted interior rods, whereas lowering the free energy of edge bound twisted rods, thus leading to the chiral control of the line tension. Likewise, chirality can also raise the line tension if the twist at the membrane's edge is the opposite of the natural twist preferred by the constituent molecules.

For achiral membranes, the line tension associated with the exposed edge of left-handed and right-handed outward protrusions is roughly equal. The overall free energy does not significantly change as one outward protrusion extends its length at the expense of another one, by translating the cusp defect. In this limit, the point defects freely diffuse and the lengths of outward protrusions with either handedness exhibit significant fluctuations in agreement with experimental observations. However, away from the achiral limit, there is a finite difference in line tension between the left-handed and right-handed outward protrusions, and the free energy is minimized by reducing the length of the outward protrusions with unfavorable twist.

To quantitatively test these ideas, we have measured the effective interaction between a pair of point defects that are connected by a single protrusion. We used phase contrast microscopy to track the positions, s_i, of two adjoining defects along the membrane contour (Fig. 5*A*). For an achiral sample ($x_{fd} = 0.26$), the separation between two adjoining defects, $\delta s = s_{i+1} - s_i$, fluctuates by many microns over a timescale of minutes (Fig. 5*B*). However, away from achiral limit, we observe that the relative separation between these defect pairs remains well defined on

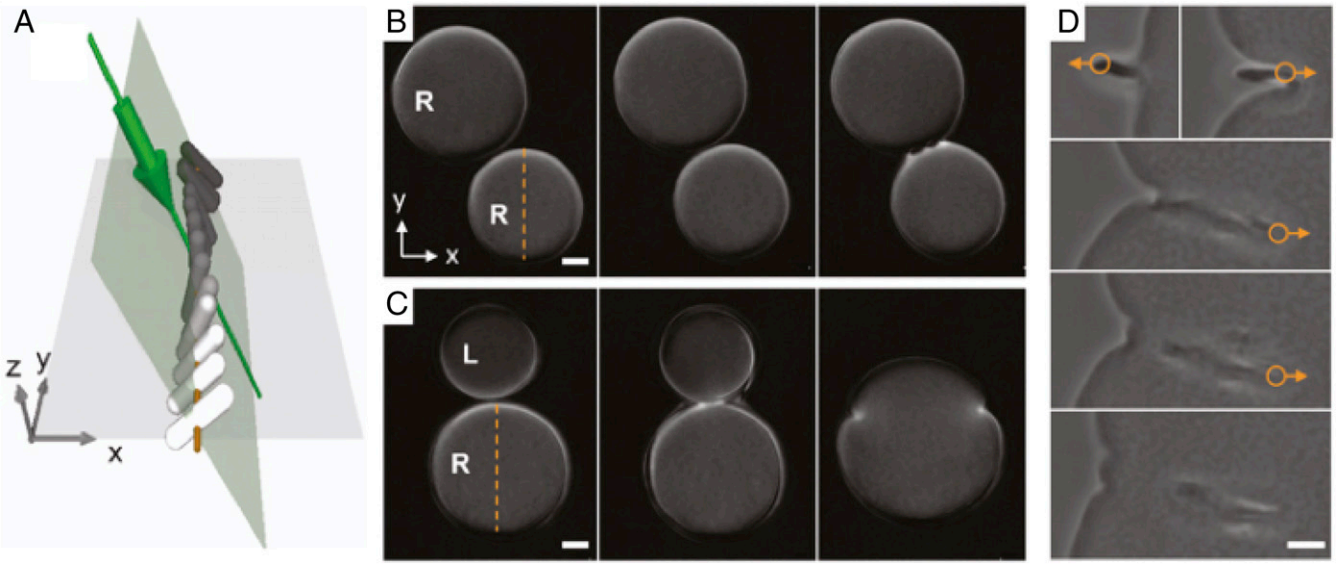

Fig. 4. Lateral coalescence of membranes with opposite chirality leads to scalloped edges. (*A*) Angled light illuminating 1D cross-section of twisted rods reveals the handedness of edge-bound rods. Because the direction of the incident light is tilted toward the *x* axis, rods twisting counterclockwise along the light source are not birefringent and appear dark. In contrast, rods twisting clockwise, away from the incoming light, have higher optical anisotropy and thus appear bright. Tilting the light source breaks the symmetry of the 2D-LC-PolScope setup and allows us to distinguish between left-handed (L) and right-handed (R) membranes with a higher spatial resolution than that of the 3D-LC-PolScope. The grayscale changes from dark to light with increasing retardance, where the rods aligned with the direction of incident light have zero retardance. (*B*) The coalescence of two right-handed membranes, which are both bright at the top and dark at the bottom, results in the formation of pores. (*C*) Coalescence of a left-handed membrane with a right-handed membrane produces two cusps that separate the left-handed edge section from the right-handed one. (*D*) An outward protrusion with a pair of defects can be imprinted into the edge using optical tweezers. The empirical method, which allows for robust engineering of cusp defects, consists of pulling the twisted ribbons out of the membrane edge and subsequently dragging it into the membrane. (Scale bars: 4 μm.)

experimental timescales. We measured the probability distribution function, $P(\delta s)$, of the defects being separated by distance δs. The measured distributions are described by a Gaussian: $P(\delta s) = \exp(-\alpha(\delta s - \delta s_0)^2/2k_BT)$, indicating that the defects are bound by a harmonic potential centered around the equilibrium separation, δs_0 (Fig. 5*C*). The equilibrium defect separation as well as the strength of the effective binding potential, α, depends on x_{fd}, the ratio of left- and right-handed rods. By varying membrane composition, we extracted how α, as well as the equilibrium separation, $\delta s_0 = <\delta s>$, depends on x_{fd} (Fig. 5 *D* and *E*). Approaching the

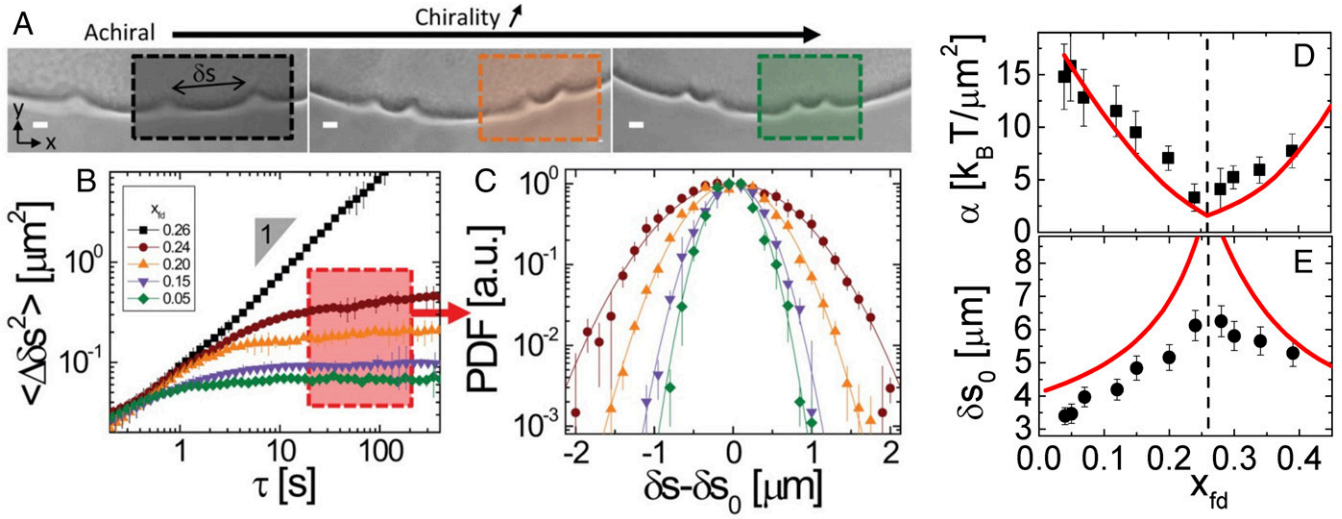

Fig. 5. Ratio of left- and right-handed rods tunes the effective defect interactions. (*A*) Phase contrast image of scalloped membranes at $C_{Dextran} = 40$ mg/mL. Number fraction is decreasing from *Left* to *Right* ($x_{fd} = 0.26$, 0.15, and 0.05). Increasing the chirality by lowering x_{fd} leads to tighter coupling between point defects due to the increasing difference in the line tension of the protrusions with left- and right-handed twist. (Scale bars: 2 μm.) The color of the shaded boxes indicates different mean-square displacement of defect separation in *B*. (*B*) Mean-square fluctuations of the separation of two coupled defects as a function of time at different x_{fd}. In the achiral case, the defects exhibit diffusive dynamics with the effective diffusion coefficient, $D = 0.04$ μm²/s. (*C*) Normalized probability distribution function (PDF), $P(\delta s - \delta s_0)$, extracted from relative separation of two defects for different values of x_{fd} taken at $\tau \sim 100$ s, where $<\Delta\delta s^2>$ plateaus (red box in *B*). $P(\delta s - \delta s_0)$ is fitted by a Gaussian distribution $\exp(-\alpha(\delta s - \delta s_0)^2/2k_BT)$. (*D*) The spring constant α of the harmonic potential around the equilibrium position δs_0 as a function of x_{fd}. (*E*) Equilibrium distance between the defects δs_0 as a function of x_{fd}.

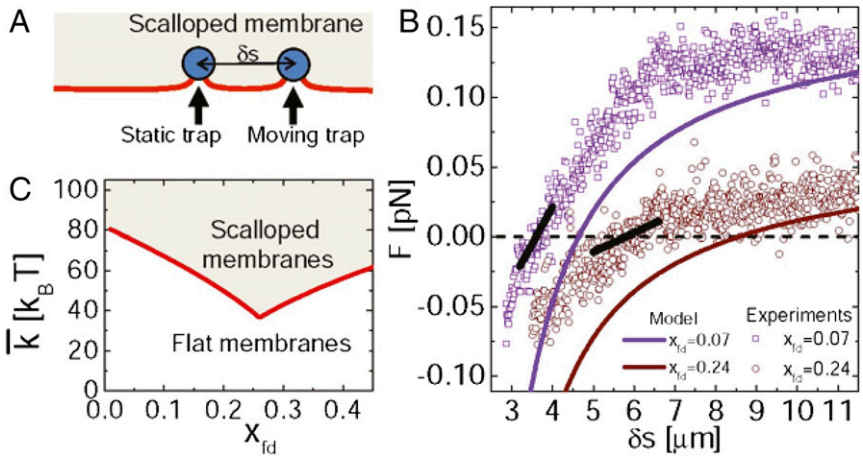

Fig. 6. Measurement of defect binding and theoretical model of scalloped membranes. (*A*) Schematic of the active experiments to measure defect interactions. Beads are embedded into defects. One defect is moved using an optical trap, and the force, *F*, exerted on the static defect is simultaneously measured. (*B*) Comparison between the force measurements (dots) obtained with laser tweezers and the theoretical model (full curves) as a function of δs, the distance between two adjacent defects. The black lines correspond to the measurements from the passive experiments (Fig. 5). (*C*) Theoretical phase diagram indicating the stability region of scalloped membranes as a function of the Gaussian modulus $\bar{k}$ versus x_{fd}. The red line is the boundary between the flat and scalloped membrane phases.

achiral mixture limit ($x_{fd} = 0.26$) leads to the increase of the mean separation δs_0 and a vanishing α. In this limit, the adjacent defects effectively decouple from each other. Increasing chirality away from the achiral limit decreases equilibrium separation and increases the coupling strength, indicating tighter defect binding. The existence of a finite equilibrium separation indicates a competition between short-range repulsion, due to elastic distortions, and long-range attraction caused by the asymmetry of the line tension associated with the edges of the opposite twist.

The passive fluctuation analysis only maps the binding potential within a few $k_B T$ around its minimum. To measure the entire binding potential, we performed active experiments where we moved one defect by δs using an optical trap, while simultaneously measuring the force F exerted on the other defect (Fig. 6 *A* and *B*). For this purpose, we embedded 1.5-μm-diameter colloidal beads into two adjoining cusp defects. Once placed there, beads remained attached to a defect for the entire duration of the experiment. To ensure that the beads do not alter the defect structure, we measured thermal fluctuations of a defect pair with and without embedded beads and found them to be identical within experimental error (Fig. S3). We then calibrated the trap to measure the zero force at the equilibrium distance δs_0 (Fig. S4) and determined the optimal laser power to measure the force F (Fig. S5). We extracted the force as a function of δs, $F(\delta s)$, which is averaged over 10 identical experiments (Fig. 6 *A* and *B*). In the vicinity of the equilibrium separation, δs_0, the force measurements quantitatively agree with the fluctuation experiments described above. As expected, the force is negative below δs_0, and positive above δs_0, confirming that δs_0 is the stable equilibrium position. The force steeply increases for small separations and saturates at large separations, indicating that a defect pair is permanently bound. The magnitude of the force plateau and the slope of the force-increasing region depend on the number fraction x_{fd}. By moving farther away from the achiral limit, we find that the equilibrium distance between bound defects δs_0 decreases. These experiments also demonstrate that the pairwise defect interactions are governed by a balance between short-range repulsion and long-range attraction.

Modeling the Interactions Between Two Adjacent Point Defects

The theoretical model of scalloped membranes has been studied previously (30). Here, we provide a quantitative comparison of this theoretical model to experimental data. To summarize, our model reduces the overall 3D geometry of the membrane to an isolated configuration around a point defect. The outward protrusions between two neighboring cusps must form via the interplay between the line tension γ, the interfacial bending rigidity k_b, and the geometrical variables associated with the overall membrane deformation. For an isolated defect, the free energy is then given by the following:

$$F_2 = \int dS\left(\bar{k}\kappa_G + \sigma\right) + \sum_{i=1,2} \oint ds_i \left(\gamma_i + k_b \kappa_{s,i}^2\right), \qquad [1]$$

where κ_G is the Gaussian curvature, $\bar{k}$ is the corresponding elastic modulus (31), and σ denotes the surface tension of the membrane. The two edge profiles (enumerated by the index i) with opposite handedness meet at the point defect and are in general different, because their curvature $\kappa_{s,i}$ and line tension γ_i can be unequal. The relaxation length of each edge from a space curve to a straight line in the monolayer plane is given by the natural length scales $\xi_i \equiv \sqrt{k_b/\gamma_i}$ ($\xi_i \sim 0.5$ μm), where k_b is the bending modulus of each edge. The bulk terms are integrated over the membrane surface with an area element dS, whereas the interfacial terms are integrated along the arc length with elements ds_i. We note that the mean curvature H of the scalloped membrane is absent in Eq. **1**, because it can only contribute to the membrane free energy when there is a finite pressure difference of the surrounding aqueous solution above and below the membrane surface. However, in the presence of the free edges, the pressure difference vanishes in equilibrium, resulting in $H = 0$, that is, a minimal surface (*Theoretical Methods*). The stability of the scalloped membrane with respect to a flat membrane is determined by the free-energy difference ΔF between the two configurations. Because we compare flat and scalloped membranes with an equal area S, the surface tension σ cancels out in ΔF. Eq. **1** and its minimization procedure by a variational analysis, which yields the spring constant (Fig. 5*D*), the equilibrium defect separation (Fig. 5*E*), and the phase diagram (Fig. 6*C*), are discussed in detail in *Theoretical Methods*.

The structure of the scalloped edge is determined by the balance between two contributions to the free energy, the line energy and the surface energy. On the one hand, the line energy suppresses the formation of outward protrusions and cusp defects, because they increase the total membrane circumference. On the other hand, each cusp defect generates negative Gaussian

curvature, which lowers the free energy of elastic deformations if the Gaussian modulus is positive and sufficiently large (30). Based on the interplay between these two contributions, our model predicts regions where scalloped membranes are more stable than flat circular membranes as a function of $\bar{k}$ and x_{fd} (Fig. 6*C*). To calculate this phase diagram, we have used theoretical fits to the experimental values for γ_1 and k_b (Fig. S1 and *Theoretical Methods*). When the number fraction of the virus mixture deviates from $x_{fd} = 0.26$, an increasing magnitude of $\bar{k}$ is required to stabilize scalloped membranes (Fig. 6*C*). The reason is that, away from the achiral limit, one of the edges (e.g., associated with γ_2) has incompatible chirality with the preferred overall handedness along the membrane boundary. Consequently, the rods along that edge tilt into a high-energy configuration, as opposed to the molecules in the adjacent outward protrusion that has lower energy (with γ_1). This leads to $\Delta\gamma \equiv \gamma_2 - \gamma_1 > 0$, that is, the overall free energy of the scalloped membranes rises, and a long-range attractive interaction between two adjoined defects emerges. The two defects, however, cannot approach very close to each other because the surface in between must then flatten, leading to a diminishing negative Gaussian curvature that in turn raises the free energy. This yields short-ranged repulsive interactions between nearby defects (30, 32). The equilibrium defect separation is determined by the competition between these two effects.

Theoretical predictions for the defects separation length, δs_0, and their coupling strength, α were fit to experimental measurements (Fig. 5 *D* and *E*; *Theoretical Methods*). The line tension γ_1 and the bending rigidity k_b were taken from experiments (Fig. S1), whereas we took $\Delta\gamma$ and $\bar{k}$ as fitting parameters. The power spectrum of the membrane edge fluctuations yields γ_1 and k_b within ∼10% error. However, because γ_2 is very close to γ_1, measurements are not precise enough to extract the effective difference between them. Thus, $\Delta\gamma$ remains a free parameter, and we assume the polynomial form $\Delta\gamma = (-115x_{fd} + 30)k_BT/\mu m$ that vanishes at $x_{fd} = 0.26$ and becomes 30 $k_BT/\mu m$ at $x_{fd} = 0$, that is, $\Delta\gamma$ stays within the bounds of experimental uncertainty. Likewise, theoretical fits to experimental curves yield the magnitude of the Gaussian modulus, $\bar{k} = 200k_BT$.

The theory quantitatively reproduces how the effective defect interactions (coupling strength α and equilibrium separation δs_0) depend on x_{fd}, thus confirming their origin: a long-range attraction due to $\Delta\gamma > 0$, and a short-range repulsion associated with membrane Gaussian curvature (Fig. 5 *D* and *E*). The modulus α as a function of x_{fd}, extracted from a linear approximation to the theoretical force-extension curves at the point where the force vanishes, qualitatively agrees with the experimental profiles (Fig. 5*D*). We note that, without the Gaussian curvature contribution, a simpler 2D theory modeling a flat and thermodynamically unstable scalloped membrane consistently yields smaller δs_0 values than those from the 3D model presented here (Fig. S6). Hence, the Gaussian curvature term with a positive modulus explains the nature of in-plane and out-of-plane deformations as well as the overall stability of the scalloped membranes. Furthermore, the model with the same parameters also reproduces the optical tweezer measurements of the effective defect interactions over a much larger range of separations (Fig. 6*B*).

Certain precautions need to be taken when interpreting the extracted magnitude of the Gaussian modulus $\bar{k} = 200k_BT$. In particular, another prediction of the model is that $\bar{k}$ is equal to the product of the in-plane protrusion amplitude A (Fig. 3*F*) and the line tension (30). This is because bigger protrusions would make the edge longer at constant γ, necessitating a higher $\bar{k}$ to stabilize the scalloped membranes. At $x_{fd} = 0.26$, when the protrusion size is 2 μm (Fig. 3*A*) and the line tension is $\gamma \sim 500k_BT/\mu m$ (Fig. S1*D*), the Gaussian modulus from this relation is found as $\bar{k} = \gamma A \sim 10^3 k_BT$. This value is almost an order of magnitude higher than $\bar{k} = 200k_BT$ extracted for the theoretical fits (Fig. 5 *D* and *E*). The resulting discrepancy between two estimates of the Gaussian modulus may be due to the fact that our model relies on a simple geometrical assumption, an axially symmetric catenoidal surface, which likely accumulates more negative Gaussian curvature than the experimental shape of the membrane surface. Therefore, our analysis underestimates the Gaussian modulus that stabilizes the scalloped membrane over a flat configuration. Theoretically, compromising axial symmetry or the smoothness of the surface around the cusp could yield a minimal saddle surface with a lower amount of the total Gaussian curvature. On the one hand, this would restore $\bar{k}$ to higher values to stabilize the scalloped membranes and resolve the discrepancy between two estimates. On the other hand, this would greatly increase the complexity of our model. We note that, experimentally, the surface around the cusp must be governed by the local matching of the rod orientations, which may indeed form a nonsmooth surface at the cusp. In this configuration, the structural relation between the Gaussian modulus, the protrusion amplitude, and the line tension must still hold, as discussed elsewhere (30).

There is a discrepancy between the experimental (Fig. 2*A*) and theoretical (Fig. 6*C*) phase diagrams because theory implies that at $\bar{k} = 200k_BT$ there exist no stable flat membranes between $x_{fd} = 0$ and $x_{fd} = 1$. There may be two main reasons underlying the difference between the theoretical and experimental stability of the scalloped membranes. First, the theoretical phase diagram is calculated by quantifying only a point defect and the membrane deformations in its neighborhood, whereas the experimental stability of the scalloped membranes is governed by the overall membrane conformation associated with multiple defects (Fig. 2*B* and Fig. 3*A*). If the number of defect pairs is less than the overall membrane circumference can support, the scalloped membrane is still stable with respect to a flat membrane but would be in a metastable state. Experimentally, this might be the case, as is evident from the defect pair evolution as a function of chirality, leaving long flat sections between two successive pairs (Fig. 5*A*). Second, we assumed that $\Delta\gamma = 30\ k_BT/\mu m$ at $x_{fd} = 0$ to fit the spring constant (Fig. 5*D*); however, $\Delta\gamma$ could be larger and could be a strongly decreasing function of x_{fd}. This would result in a steeper phase boundary away from $x_{fd} = 0$, and an overall stabilization of flat monolayers away from the achiral limit.

Theoretical Estimate of Gaussian Curvature Modulus

A simple argument can be used to estimate the Gaussian curvature modulus, $\bar{k}$, of colloidal membranes of thickness D, surrounded by the depleting polymers with radius of gyration, R_g. We assume that the polymers behave as an Asakura–Osawa ideal gas of particles with effective diameter d, which is related to polymer radius of gyration by the following: $d = 4R_g/\sqrt{\pi}$. There are two distinct contributions to $\bar{k}$: an intrinsic contribution arising from the internal stresses among the virus particles $\bar{k}_m$, and an entropic contribution arising from the polymer depletants $\bar{k}_p$. First, we consider the intrinsic contribution. Because it is fluid, we assume that the membrane middle surface membrane does not stretch when the membrane bends. The rods can adjust around each other to accommodate a change in curvature without changing their equilibrium spacing in the midplane. However, imposing any curvature onto a membrane will induce a strain that depends on z, the distance along the membrane normal away from the midplane. In particular, if the membrane has mean curvature H and Gaussian curvature κ_G, then the areal strain of the surface at distance z is given by $\varepsilon(z) = 2Hz + \kappa_G z^2$ (33). The corresponding lateral membrane stress is $\sigma(z) = \sigma_0(z) + Y\varepsilon(z)$, where $\sigma_0(z)$ is the stress in the membrane when it is flat, and Y is the modulus for areal compression. Because the rods are uniform along their lengths, we take Y to be independent of z. The lateral stress is isotropic because the membrane is fluid. There is a compressive stress in the membrane even when it is flat because the polymer depletants squeeze the membrane (34). The total volume excluded

to the polymers for a flat membrane of area A is $V_{0,ex} = A(D+d)$, leading to a contribution to the free energy per unit area $\gamma = nk_BT(D+d)$, which can also be considered an entropic tension (16). n is polymer concentration. To balance this tension, the rods must experience a compressive stress $\sigma_0(z) = -n\ k_BT(D+d)/D$. To calculate the contribution to $\bar{k}$ from the rods in the membrane with zero mean curvature, we write the membrane free energy per unit mid-surface by integrating the stress with the respect to the strain as $\mathcal{F}_m = \int_{-D/2}^{D/2} dz \int_0^{\varepsilon(z)} d\varepsilon' \sigma(\varepsilon') = \bar{k}_m \kappa_G$, where $\bar{k}_m = \int_{-D/2}^{D/2} dz\ z^2 \sigma_0(z)$ (17, 35). The intrinsic contribution to the Gaussian curvature modulus is always negative, $\bar{k}_m = -nk_BT(D+d)D^2/12$. Next, we consider the contribution of the depleting polymer to the total free energy of the system. In general, as the membrane assumes a curved configuration, the volume excluded to the depleting polymer will change from $V_{0,ex}$. Specifically,, for a membrane with zero-mean curvature: $V_{ex} = \int dA \int_{-(D+d)/2}^{(D+d)/2} (1+\kappa_G z^2) dz$. Consequently, a membrane that goes from a flat state to a configuration with a negative Gaussian curvature will be accompanied with the decrease in the volume excluded to the depletant polymers and, thus, will increase the overall system entropy. This excluded volume effect introduces a positive contribution to the Gaussian modulus. Integrating across the membrane thickness and using $F_p = nk_BTV_{ex} = \gamma A + \bar{k}_p \int dA \kappa_G$ yields $\bar{k}_p = (D+d)^3 nk_BT/12$. The net Gaussian curvature modulus is therefore $\bar{k} = \bar{k}_p + \bar{k}_m \approx D^2 dnk_BT/6$, where the approximation follows because the membrane is much thicker than the polymer particles, $D >> d$.

To estimate the polymer contribution to the Gaussian curvature modulus, we use $n \sim 40$ mg/mL, $D \sim 880$ nm, and $d \sim 30$ nm for a dextran with molecular weight of 500,000 g/mol (36). With these numbers, we find that $\bar{k} \sim 185\ k_BT$. Despite its approximate nature, our estimate yields the magnitude $\bar{k}$ that is in reasonable agreement with experimental measurements. Note that our argument for the polymer contribution is similar to the model put forward to explain negative Gaussian curvature modulus for surfactant interfaces: for a saddle-splay surface with $H = 0$, there is less room for the surfactant chains, which therefore must stretch and incur a higher free energy (37).

Discussions and Conclusions

Our combined theoretical and experimental work demonstrates that membranes composed of achiral rods exhibit higher structural complexity compared with flat membranes assembled from chiral rod-like viruses. In the latter case, strong chirality enforces uniform twist of rods along the entire membrane circumference, leading to the formation of flat 2D disks. By contrast, weakly chiral or achiral membranes exhibit an intriguing instability that is driven by an interplay between the Gaussian curvature of a colloidal membrane and the spontaneous achiral symmetry breaking of rods located at the membrane's edge. The achiral symmetry breaking induces formation of cusp-like defects. These defects in turn allow the membrane to adopt a 3D shape that decreases the overall energy associated with its negative Gaussian curvature.

Despite the important role it plays in diverse processes, measuring the Gaussian modulus of conventional lipid bilayers remains a significant experimental challenge. In comparison, the properties of the colloidal membranes described here allow us to estimate their Gaussian modulus. Conventional bilayers have a negative Gaussian modulus, which means that saddle-shaped deformations increase the membrane energy (7, 10, 11, 38). On the contrary, experiments described here, as well as previous observations of diverse assemblages with excess Gaussian curvatures such as arrays of pores and twisted ribbons (19, 26), demonstrate that colloidal monolayers, in contrast to lipid bilayers, have positive Gaussian moduli.

Achiral symmetry breaking has been observed in diverse soft systems with orientational order, ranging from lipid monolayers and nematic tactoids to confined chromonic liquid crystals (39–45). In particular, the measured structure and interactions of the cusp-like defects in colloidal membranes resemble studies of point defects moving along a liquid crystalline dislocation line in the presence of chiral additives (46). The main difference is that in the colloidal membranes the achiral symmetry breaking leads to out-of-plane 3D membrane distortions that couples liquid crystal physics to membrane deformations. This is not possible for inherently confined liquid crystalline films.

From an entirely different perspective, a number of emerging techniques have been developed to fold, wrinkle, and shape thin elastic sheets with in-plane elasticity (47–50). So far, these efforts were focused on studying instability of thin elastic films with finite in-plane shear modulus. The methods to achieve folding or wrinkling of thin sheets involves either engineering of in-plane heterogeneities or imposing an external force. Our work demonstrates that simpler uniform elastic sheets lacking in-plane rigidity can spontaneously assume complex 3D folding patterns that decorate its edge.

Finally, methods described here and in our previous work should be applicable to any monodisperse rod type with sufficiently large aspect ratio. Thus, they might offer a scalable method for robust assembly of photovoltaic devices composed of nanorods. Our previous investigation of chiral *fd-wt* colloidal membranes demonstrated that the twist at their edges introduces a significant energetic barrier that suppresses their lateral coalescence (26). In such samples, membranes with diameters ranging from 10 to 100 μm are commonly found. Compared with chiral colloidal membranes, we find that colloidal membranes of monodisperse virus mixtures that are close to the achiral limit coalesce much faster and can easily reach millimeter dimensions.

Materials and Methods

Sample Preparation. Both viruses, *fd* and *fd*-Y21M, were grown in bacteria and purified as described elsewhere (19). *fd*-Y21M, has a single point mutation in the amino acid sequence of the major coat protein: amino acid number 21 is replaced from Y to M. *fd* and *fd*-Y21M were labeled with fluorescent dye as described elsewhere (51). The preparation of optical chambers was described elsewhere (19).

Optical Microscopy. Experiments were carried out on an inverted microscope (Nikon TE 2000) equipped with traditional polarization optics, a differential interference contrast (DIC) module, a fluorescence imaging module, and 2D-LC-Polscope module. For dual-view fluorescence imaging, we used DV2 from Photometrics. We used a 100× oil-immersion objective (PlanFluor, N.A. 1.3, for DIC and PlanApo, N.A. 1.4, for phase contrast). Images were recorded with cooled CCD cameras [CoolSnap HQ (Photometrics) or Retiga Exi (QImaging)]. For 3D-LC-PolScope measurements, we used a Zeiss Axiovert 200M microscope with a Plan Apochromat oil-immersion objective (63×/1.4 N.A.) and a monochrome CCD camera (Retiga 4000R; QImaging).

Laser Tweezers. A 1,064-nm laser (Coherent Compass) was brought into the optical path of an inverted microscope (Nikon Eclipse Te2000-u) and focused with a 100× objective onto the image plane (Nikon PlanFlour, N.A. 1.3). To simultaneously trap multiple beads, a single beam was time shared between different positions using an acousto-optic deflector (IntraAction-276HD) (52). Bead position was measured using back focal plane interferometry and a quadrant photodiode (QPD) (53). A separate 830-nm laser (Point Source Iflex-2000) was used as a detection beam. To calibrate the photodiode, we scan a bead across the detection beam in known step sizes and measure the corresponding voltage change. Trap stiffness was calibrated by analyzing the power spectrum of the bead position (53).

ACKNOWLEDGMENTS. We acknowledge conversations with William Irvine, Robert Pelcovits, and Leroy Jia. We also acknowledge use of Brandeis Materials Research Science and Engineering Centers (MRSEC) optical and biomaterial synthesis facility supported by National Science Foundation (NSF) Grant MRSEC-1420382. T.G. acknowledges the Agence National de la Recherche Française (Grant ANR-11-PDOC-027) for support. P.S., C.N.K., R.B.M., and Z.D. acknowledge support of NSF through Grants MRSEC-1420382 and NSF-DMR-1609742. T.R.P. acknowledges support of the NSF through Grants MRSEC-1420382 and NSF-CMMI-1634552. R.D.K. was partially supported by a Simons Investigator grant and Grant NSF-DMR-1262047.

1. Lipowsky R (1991) The conformation of membranes. *Nature* 349:475–481.
2. Seifert U (1997) Configurations of fluid membranes and vesicles. *Adv Phys* 46:13–137.
3. Kamien RD (2002) The geometry of soft materials: A primer. *Rev Mod Phys* 74:953.
4. Evans E, Rawicz W (1990) Entropy-driven tension and bending elasticity in condensed-fluid membranes. *Phys Rev Lett* 64:2094–2097.
5. Brochard F, Lennon J (1975) Frequency spectrum of the flicker phenomenon in erythrocytes. *J Phys* 36:1035–1047.
6. Rawicz W, Olbrich KC, McIntosh T, Needham D, Evans E (2000) Effect of chain length and unsaturation on elasticity of lipid bilayers. *Biophys J* 79:328–339.
7. Hu M, Briguglio JJ, Deserno M (2012) Determining the Gaussian curvature modulus of lipid membranes in simulations. *Biophys J* 102:1403–1410.
8. Hu M, Diggins P, Deserno M (2013) Determining the bending modulus of a lipid membrane by simulating buckling. *J Chem Phys* 138:214110.
9. Siegel DP (2008) The Gaussian curvature elastic energy of intermediates in membrane fusion. *Biophys J* 95:5200–5215.
10. Semrau S, Idema T, Holtzer L, Schmidt T, Storm C (2008) Accurate determination of elastic parameters for multicomponent membranes. *Phys Rev Lett* 100:088101.
11. Baumgart T, Das S, Webb WW, Jenkins JT (2005) Membrane elasticity in giant vesicles with fluid phase coexistence. *Biophys J* 89:1067–1080.
12. Barry E, Dogic Z (2010) Entropy driven self-assembly of nonamphiphilic colloidal membranes. *Proc Natl Acad Sci USA* 107:10348–10353.
13. Kaplan CN, Tu H, Pelcovits RA, Meyer RB (2010) Theory of depletion-induced phase transition from chiral smectic-A twisted ribbons to semi-infinite flat membranes. *Phys Rev E Stat Nonlin Soft Matter Phys* 82:021701.
14. Yang Y, Barry E, Dogic Z, Hagan MF (2012) Self-assembly of 2D membranes from mixtures of hard rods and depleting polymers. *Soft Matter* 8:707–714.
15. Kaplan CN, Meyer RB (2014) Colloidal membranes of hard rods: Unified theory of free edge structure and twist walls. *Soft Matter* 10:4700–4710.
16. Kang L, Gibaud T, Dogic Z, Lubensky TC (2016) Entropic forces stabilize diverse emergent structures in colloidal membranes. *Soft Matter* 12:386–401.
17. Helfrich W (1974) The size of bilayer vesicles generated by sonication. *Phys Lett A* 50: 115–116.
18. Barry E, Dogic Z, Meyer RB, Pelcovits RA, Oldenbourg R (2009) Direct measurement of the twist penetration length in a single smectic A layer of colloidal virus particles. *J Phys Chem B* 113:3910–3913.
19. Gibaud T, et al. (2012) Reconfigurable self-assembly through chiral control of interfacial tension. *Nature* 481:348–351.
20. Purdy KR, et al. (2003) Measuring the nematic order of suspensions of colloidal fd virus by x-ray diffraction and optical birefringence. *Phys Rev E Stat Nonlin Soft Matter Phys* 67:031708.
21. Rosay M, et al. (2001) Sensitivity-enhanced NMR of biological solids: Dynamic nuclear polarization of Y21M fd bacteriophage and purple membrane. *J Am Chem Soc* 123: 1010–1011.
22. Pouget E, Grelet E, Lettinga MP (2011) Dynamics in the smectic phase of stiff viral rods. *Phys Rev E Stat Nonlin Soft Matter Phys* 84:041704.
23. Tombolato F, Ferrarini A, Grelet E (2006) Chiral nematic phase of suspensions of rodlike viruses: Left-handed phase helicity from a right-handed molecular helix. *Phys Rev Lett* 96:258302.
24. Barry E, Beller D, Dogic Z (2009) A model liquid crystalline system based on rodlike viruses with variable chirality and persistence length. *Soft Matter* 5:2563–2570.
25. Dogic Z, Fraden S (2000) Cholesteric phase in virus suspensions. *Langmuir* 16: 7820–7824.
26. Zakhary MJ, et al. (2014) Imprintable membranes from incomplete chiral coalescence. *Nat Commun* 5:3063.
27. Oldenbourg R, Mei G (1995) New polarized light microscope with precision universal compensator. *J Microsc* 180:140–147.
28. Oldenbourg R (2008) Polarized light field microscopy: An analytical method using a microlens array to simultaneously capture both conoscopic and orthoscopic views of birefringent objects. *J Microsc* 231:419–432.
29. Sharma P, Ward A, Gibaud T, Hagan MF, Dogic Z (2014) Hierarchical organization of chiral rafts in colloidal membranes. *Nature* 513:77–80.
30. Kaplan CN, Gibaud T, Meyer RB (2013) Intrinsic curvature determines the crinkled edges of "crenellated disks." *Soft Matter* 9:8210–8215.
31. Deuling HJ, Helfrich W (1976) The curvature elasticity of fluid membranes: A catalogue of vesicle shapes. *J Phys* 37:1335–1345.
32. Tu H, Pelcovits RA (2013) Theory of self-assembled smectic-A crenellated disks: Membranes with cusped edges. *Phys Rev E Stat Nonlin Soft Matter Phys* 87:032504.
33. Safran SA (1994) *Statistical Thermodynamics of Surfaces, Interfaces, and Membranes* (Perseus Books, Cambridge, MA).
34. Asakura S, Oosawa F (1954) On interaction between two bodies immersed in a solution of macromolecules. *J Chem Phys* 22:1255–1256.
35. Szleifer I, Kramer D, Ben-Shaul A, Gelbart WM, Safran S (1990) Molecular theory of curvature elasticity in surfactant films. *J Chem Phys* 92:6800–6817.
36. Senti FR, et al. (1955) Viscosity, sedimentation, and light-scattering properties of fraction of an acid-hydrolyzed dextran. *J Polym Sci, Polym Phys Ed* 17:527–546.
37. Milner S, Witten T (1988) Bending moduli of polymeric surfactant interfaces. *J Phys* 49:1951–1962.
38. Siegel DP, Kozlov MM (2004) The gaussian curvature elastic modulus of N-monomethylated dioleoylphosphatidylethanolamine: Relevance to membrane fusion and lipid phase behavior. *Biophys J* 87:366–374.
39. Viswanathan R, Zasadzinski JA, Schwartz DK (1994) Spontaneous chiral-symmetry breaking by achiral molecules in a Langmuir-Blodgett-film. *Nature* 368:440–443.
40. Link DR, et al. (1997) Spontaneous formation of macroscopic chiral domains in a fluid smectic phase of achiral molecules. *Science* 278:1924–1927.
41. Hough LE, et al. (2009) Helical nanofilament phases. *Science* 325:456–460.
42. Hough LE, et al. (2009) Chiral isotropic liquids from achiral molecules. *Science* 325: 452–456.
43. Tortora L, Lavrentovich OD (2011) Chiral symmetry breaking by spatial confinement in tactoidal droplets of lyotropic chromonic liquid crystals. *Proc Natl Acad Sci USA* 108: 5163–5168.
44. Jeong J, Davidson ZS, Collings PJ, Lubensky TC, Yodh AG (2014) Chiral symmetry breaking and surface faceting in chromonic liquid crystal droplets with giant elastic anisotropy. *Proc Natl Acad Sci USA* 111:1742–1747.
45. Jeong J, et al. (2015) Chiral structures from achiral liquid crystals in cylindrical capillaries. *Proc Natl Acad Sci USA* 112:E1837–E1844.
46. Zywociński A, Pawlak K, Hołyst R, Oswald P (2005) Chirality-biased point defects dynamics on a disclination line in a nematic liquid crystal. *J Phys Chem B* 109:9712–9718.
47. Cerda E, Mahadevan L (2003) Geometry and physics of wrinkling. *Phys Rev Lett* 90: 074302.
48. King H, Schroll RD, Davidovitch B, Menon N (2012) Elastic sheet on a liquid drop reveals wrinkling and crumpling as distinct symmetry-breaking instabilities. *Proc Natl Acad Sci USA* 109:9716–9720.
49. Pocivavsek L, et al. (2008) Stress and fold localization in thin elastic membranes. *Science* 320:912–916.
50. Leocmach M, Nespoulous M, Manneville S, Gibaud T (2015) Hierarchical wrinkling in a confined permeable biogel. *Sci Adv* 1:e1500608.
51. Lettinga MP, Barry E, Dogic Z (2005) Self-diffusion of rod-like viruses in the nematic phase. *Europhys Lett* 71:692.
52. Molloy JE (1998) Optical chopsticks: Digital synthesis of multiple optical traps. *Methods Cell Biol* 55:205–216.
53. Allersma MW, Gittes F, deCastro MJ, Stewart RJ, Schmidt CF (1998) Two-dimensional tracking of ncd motility by back focal plane interferometry. *Biophys J* 74:1074–1085.
54. Zhong-can OY, Helfrich W (1989) Bending energy of vesicle membranes: General expressions for the first, second, and third variation of the shape energy and applications to spheres and cylinders. *Phys Rev A Gen Phys* 39:5280–5288.
55. Kaplan CN (2012) Colloidal membranes: The rich confluence of geometry and liquid crystals. PhD thesis (Brandeis University, Waltham, MA).
56. Millman RS, Parker GD (1977) *Elements of Differential Geometry* (Prentice-Hall, Englewood Cliffs, NJ).
57. Nitsche J (1989) *Lectures on Minimal Surfaces* (Cambridge Univ Press, Cambridge, UK), pp 23–24.
58. Stoker J (1969) *Differential Geometry* (Wiley, New York).
59. Forsythe GE, Moler CB, Malcolm MA (1976) *Computer Methods for Mathematical Computations* (Prentice-Hall, Englewood Cliffs, NJ).